Int J Adv Manuf Technol (2015) 79:645–655
DOI 10.1007/s00170-015-6852-5

ORIGINAL ARTICLE

Error map construction and compensation of a NC lathe under thermal and load effects

Sitong Xiang · Jianguo Yang

Received: 24 September 2014 / Accepted: 27 January 2015 / Published online: 13 February 2015

Abstract Thermally induced errors and load-induced errors are two key factors affecting the accuracy of machine tools. This paper proposes a strategy to build an error map of a machine tool by considering both thermal and load effects. A moderation model is developed to analyze the positioning errors with thermal effects, and a Fourier series model is used to fit the straightness errors. Based on actual cutting tests, relationships between cutting forces and motor currents are established. A load test is conducted in which a pushing cylinder is used to simulate actual cutting forces. The changes in error motions under different loads are obtained. An experimental verification is conducted on an NC lathe, whose error map is generated by integrating thermal and load effects. As actual cutting results show, when thermal and load effects are simultaneously compensated, the machining accuracy increases by 10 % as compared with when only thermal effects are compensated.

Keywords Machine tool · Error modeling · Error compensation · Thermal effect · Load effect

1 Introduction

The demand for high accuracy of machine tools is increasing. For a machine tool, the principal sources of error are geometric, cutting force-induced, fixture-dependent, and thermal errors [1]. The synthesized effect of these errors on the machine tool is called an error map. Building the error map of a machine tool is crucial in compensating for the volumetric error of the working space. The homogeneous transfer matrix (HTM) method is a widely used mathematical strategy to build the error map.

In a machine tool, thermal errors are a major part of quasistatic errors, comprising 70 % of the total error. In recent decades, various researchers have focused on the development of thermal error models by using different modeling methodologies, such as artificial neural networks [2, 3], multiple linear regression method [4, 5], and finite element method [6, 7]. It is crucial to integrate the thermal effects into the volumetric error model. Zhang [8] provided a modeling method for the volumetric error of five-axis machine tools. He classified 37 errors on a five-axis machine tool into three categories: functional, random, and negligible errors. Liu [9] considered thermal drift errors and used 30 geometric errors to model the volumetric error.

Load-induced error is another significant factor influencing machining accuracy. Furukawa [10] analyzed the contact deformation of slides during loading. Yang [11] developed a real-time error compensation system to reduce the cutting force-induced planar error of a two-axis turning center by using sensing and computer control techniques. Wu [12] modeled the cutting force by motor current and used a back propagation neural network and a genetic algorithm to predict the cutting force-induced error for an NC twin-spindle lathe. Fan [13] proposed a mathematical model to calculate the geometric errors of slides due to contact deformations caused by the wear of the guideway and then to predict the positioning errors after long-term operation.

However, in recent research, few have integrated the thermal and load effects into the error map. Because of their importance to machining accuracy, this study constructs the error map under both effects. In Section 2, the kinematic model of a machine tool is built using the HTM method. Component errors with thermal effects are modeled in Section 3. Then, the displacement of the spindle and error motions of the slide due to the load effects are analyzed in Section 4. Finally, in

S. Xiang (✉) · J. Yang
School of Mechanical Engineering, Shanghai Jiao Tong University, Shanghai 200240, People's Republic of China
e-mail: stone.xiangst@gmail.com

Section 5, both the thermal and load effects are integrated into the kinematic model, and experimental implementations are conducted.

2 Synthesized error model establishment

This research is conducted on an NC lathe, whose structure is depicted in Fig. 1. The lathe has two axes, namely the *X*- and *Z*-axes. The *X*-axis is mounted on the *Z*-axis in the form of a dovetail bracket, while the *Z*-axis is mounted on the guideway with one side with the triangle constraint and the other side with the plane constraint. The coordinate systems are established as shown in Fig. 1. The reference coordinate system (RCS) is set on the machine coordinate system. The spindle coordinate system (SCS) is set on the spindle and moves with thermal shifts. The carriage coordinate system (CCS) is located on the carriage of the *Z*-axis and moves with the *Z*-axis. The tool coordinate system (TCS) is located on the turret and moves with the *X*-axis.

All the errors of the tested lathe are in the *XZ* plane. There are 14 major errors influencing the accuracy of the machine tool. These errors are listed as follows:

(1) *Z*-axis: positioning error δ_{zz}, straightness error δ_{xz}, yaw error $\varepsilon_{\beta z}$, and two thermal shifts of CCS relative to RCS in the *X* and *Z* directions, namely, Δrc_x and Δrc_z.
(2) *X*-axis: positioning error δ_{xx}, straightness error δ_{zx}, yaw error $\varepsilon_{\beta x}$, and two thermal shifts of TCS relative to CCS in the *X* and *Z* directions, namely, Δct_x and Δct_z.
(3) Spindle: the parallelism error η_{sz} between the spindle and the *Z*-axis and two thermal shifts of the spindle in the *X* and *Z* directions, namely, Δrs_x and Δrs_z. η_{sz} can be measured by a dial indicator moving along the *Z*-axis. Thermal shifts of the spindle can be measured by various methods. The authors have also proposed an effective modeling method [14].

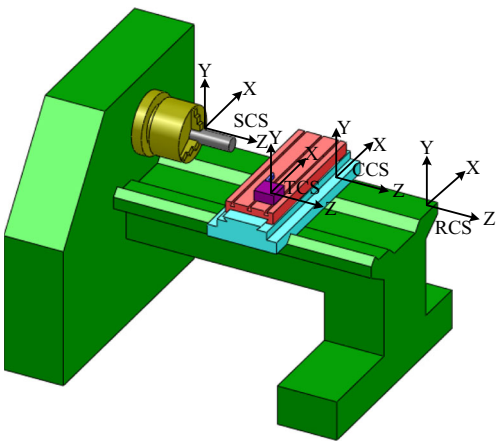

Fig. 1 Configuration and coordinate system establishment of the machine tool

(4) The squareness error between the *X*- and *Z*-axes η_{xz}.

$\mathbf{T}_r(t)$, the position of the cutting point in the RCS, is described in Eq. (1).

$$\mathbf{T}_r(t) = \mathbf{T}_r^c \cdot \mathbf{T}_c^t \cdot \mathbf{T}_t(t) \tag{1}$$

where $\mathbf{T}_c^t$ denotes the HTM from TCS to CCS, $\mathbf{T}_r^c$ indicates the HTM from CCS to RCS, and $\mathbf{T}_t(t) = [\,T_z \quad T_x \quad 1\,]^T$ is the position of the cutting point in TCS.

The workpiece size in RCS is presented in Eq. (2):

$$(W + \Delta W)_r = \mathbf{T}_r^s (W + \Delta W)_s \tag{2}$$

where W is the ideal workpiece size, and ΔW is the size error; $\mathbf{T}_r^s$ is the HTM from SCS to RCS; and $(W+\Delta W)_s$ is the actual workpiece size in the SCS.

In the actual cutting process, the cutting point of the tool and the workpiece is the same; therefore, Eq. (3) is obtained.

$$\mathbf{T}_r^s (W + \Delta W)_s = \mathbf{T}_r^c \cdot \mathbf{T}_c^t \cdot \mathbf{T}_t(t) \tag{3}$$

The detailed expressions of the HTMs in Eq. (3) are presented in Eqs. (4–6).

$$\mathbf{T}_r^s = \begin{bmatrix} 1 & -\eta_{rs} & \Delta rs_z \\ \eta_{rs} & 1 & \Delta rs_x \\ 0 & 0 & 1 \end{bmatrix} \tag{4}$$

where η_{rs} is the parallelism between the spindle and the reference axis *Zr*.

$$\mathbf{T}_r^c = \begin{bmatrix} 1 & -\varepsilon_{\beta z} & \delta_{zz} + z + \Delta rc_z + Mrc_z \\ \varepsilon_{\beta z} & 1 & \delta_{xz} + z\eta_{rz} + \Delta rc_x + Mrc_x \\ 0 & 0 & 1 \end{bmatrix} \tag{5}$$

where η_{rz} is the parallelism between the *Z*-axis and the reference axis *Zr*. Mrc_x and Mrc_z are the *X* and *Z* positions of CCS in RCS, respectively.

$$\mathbf{T}_c^t = \begin{bmatrix} 1 & -\varepsilon_{\beta x} & \delta_{zx} - x \cdot \eta_{rx} + \Delta ct_z + Mct_z \\ \varepsilon_{\beta x} & 1 & \delta_{xx} + x + \Delta ct_x + Mct_x \\ 0 & 0 & 1 \end{bmatrix} \tag{6}$$

where Mct_x and Mct_z are the *X* and *Z* positions of TCS in CCS, respectively. η_{rx} presents the squareness error between the *X*-axis and the reference axis *Zr*. The relationships between these

parallelisms are as follows:

$$\eta_{sz} = \eta_{rz} - \eta_{rs}, \eta_{sx} = \eta_{rx} - \eta_{rs} \tag{7}$$

Substituting Eqs. (4–6) into Eq. (3), the error vector ΔW is obtained in Eq. (8).

$$\begin{aligned} \Delta W_z = {} & \delta_{zx} + \delta_{zz} - (\eta_{sx} + \varepsilon_{\beta z})x - (\varepsilon_{\beta z} + \varepsilon_{\beta x} - \eta_{rs})T_x - (\varepsilon_{\beta z} - \eta_{rs}) \\ & Mct_x + Mrc_x\eta_{rs} + \Delta st_z \Delta W_x = \delta_{xx} + \delta_{xz} - \eta_{sz}z + \\ & (\varepsilon_{\beta z} + \varepsilon_{\beta x} - \eta_{rs})T_z - (\varepsilon_{\beta z} - \eta_{rs})Mct_z + Mrc_z\eta_{rs} + \Delta st_x \end{aligned} \tag{8}$$

where $\Delta st_z = \Delta rc_z + \Delta ct_z - \Delta rs_z$, and $\Delta st_x = \Delta rc_x + \Delta ct_x - \Delta rs_x$. Δst is the displacement between the tool and workpiece due to thermal effects. In the test, Δst is obtained by installing displacement sensors on the spindle. When the load effects are considered, the error vector ΔW is updated as shown in Eq. (9).

$$\begin{aligned} \Delta W_z' &= \Delta W_z{}^{T+L} + \delta_{\text{F-spindle-z}} \\ \Delta W_x' &= \Delta W_x{}^{T+L} + \delta_{\text{F-spindle-x}} \end{aligned} \tag{9}$$

where $\Delta W_x{}^{T+L}$ and $\Delta W_z{}^{T+L}$ are the error vectors generated by new models of component errors under thermal and load effects. Parameters $\delta_{\text{F-spindle-x}}$ and $\delta_{\text{F-spindle-z}}$ represent spindle shift errors in the X and Z directions caused by the loads, respectively.

The flowchart of the error vector generation is shown in Fig. 2. Two tests, namely the thermal test and the load test, are conducted in Sections 3 and 4, respectively. In the thermal test, models of component errors under thermal effects are presented. Similarly, in the load test, the load-induced errors, namely spindle shift errors and component errors under load effects are analyzed.

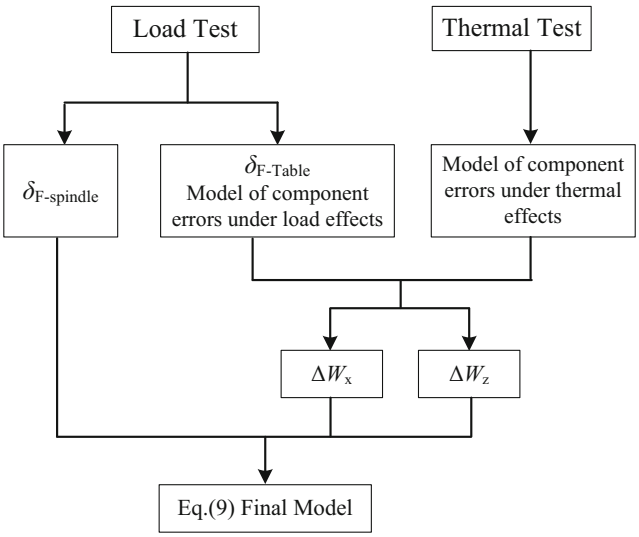

Fig. 2 Flowchart of error map generation

3 Modeling of component errors under thermal effects

To generate the error map, it is necessary to input the models of the component errors into the error vector described in Eq. (8). Common component errors are positioning errors, straightness errors, squareness errors, and angular deviations. The positioning errors are significantly affected by thermal effects, but the straightness errors are not significantly affected by temperature variations [15]. In this section, several novel methods of modeling component errors are demonstrated.

To model the thermal errors, temperature sensors are arranged on the machine tool. The locations of the temperature sensors are listed in Table 1. The arrangement of the temperature sensors on the ball screw is presented in Fig. 3.

3.1 Moderation model for positioning errors

Accounting for 40–70 % of the total machine tool errors [1, 16], positioning errors of translational axes are one of the most significant factors affecting the machine tool accuracy. Positioning errors are both position and thermal dependent. Figure 4 presents that the positioning errors vary significantly with positions and thermal conditions. From Fig. 4, the thermal effects influence the slopes of the error curves but cause little change in their forms.

Moderation occurs when the relationship between two variables depends on a third variable. The third variable is referred to as the moderator variable or simply the moderator [17]. Here, the two variables are the positioning error and the position, and the third variable is the thermal factor, which is regarded as the moderator. The moderation modeling procedure is illustrated as follows.

Firstly, the error curve in normal thermal status can be fitted by a regression function:

$$y = f(x) \tag{10}$$

Table 1 Temperature sensor locations

Temperature variable	Location
t_{amb}	Ambient air
t_{xb1}, t_{xb2}	The front and rear bearings of the X-axis ball screw
t_{xn1}	The nut of the X-axis
t_{zb1}, t_{zb2}	The front and rear bearings of the Z-axis ball screw
t_{zn1}	The nut of the Z-axis
t_{sb1}, t_{sb2}	The front and rear bearings of the spindle

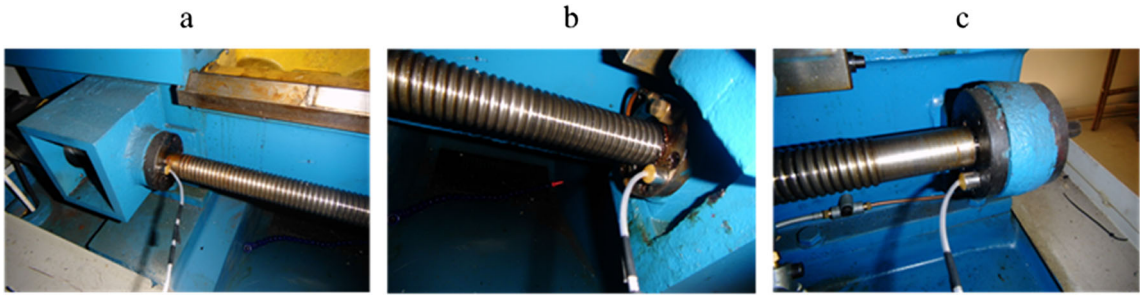

Fig. 3 Arrangement of the temperature sensors: **a** front bearing, **b** nut, and **c** rear bearing

where, y is the criterion variable, namely the positioning error; x is the predictor variable, namely the position.

Secondly, the thermal moderator T is added. For the error curves presented in Fig. 4, whose slopes change with different thermal status while the forms keep unchanged, it can be considered that the slope is a function of moderator T. This type of moderator is not related to either the predictor variable x or the criterion variable y. Rather, it interacts with the predicted variable x to modify the form of the relationship between x and y. This type of moderator is called pure moderator [18] and the moderation model is shown in Eq. (11).

$$y = f(x) + aTx \tag{11}$$

However, if the forms of the error curves significantly change with the thermal factor, it can be concluded that the moderator not only interacts with the predictor variable but also is a predictor variable itself. This type of moderator is called quasi moderator [18], and the moderation model can be obtained as follows.

$$y = f(x) + aT + bTx \tag{12}$$

Then, the moderator is determined by selecting the key thermal points. For a translational guideway, there are some key thermal sources: environment, motor, screw nut, and screw seat. Theoretically, each temperature can be set as a moderator. However, two or more moderators will generate lots of interaction items, and the final moderation model will be quite complicated. It is a better choice to select the most relevant thermal points by the correlation analysis or obtain an average form.

Finally, all the coefficients a and b are calculated by the least squares method. The Matlab also provides the related function packages for moderation analysis.

3.2 Modeling method for straightness errors

Besides the positioning errors, straightness errors are also extremely crucial error sources to precision manufacturing, especially in large machine tools [19]. So, it is significant to build the error model of straightness errors of translational axes.

Because of various mechanical structures, preload adjustment, guide wear, and various temperature field distributions, straightness errors show different characteristics. As shown in Fig. 5, the wave type is the most common form of straightness errors. This type of straightness error is periodic to a certain extent. Therefore, it can be approximated by a three- or four-order Fourier series as in Eq. (13). Higher order Fourier series may result in complicated mathematical expressions and even cause the problem of over-fitting. Taking the volatility of the curve into consideration, white test should be taken to

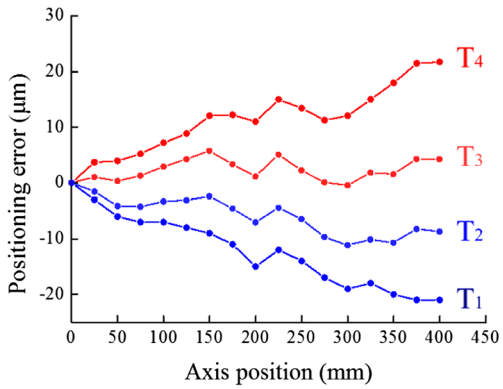

Fig. 4 Positioning errors under different temperatures

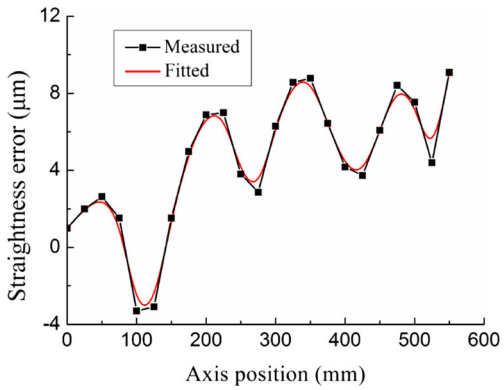

Fig. 5 Straightness error: wave type

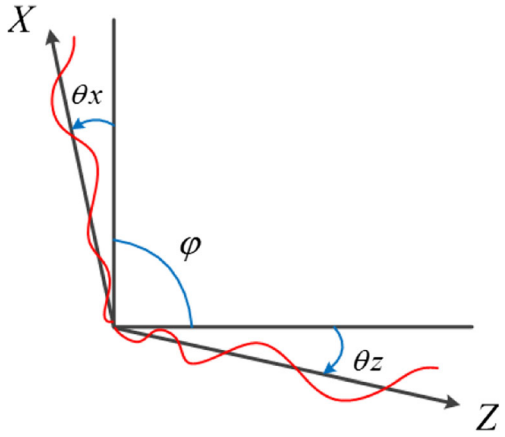

Fig. 6 Calculate method of squareness

determine whether or not the heteroscedasticity exists after modeling. If the heteroscedasticity exists, the least squares will be needed to modify the model.

$$\Delta x = a_0 + \sum_{n=1}^{4} (a_n \sin nx + b_n \cos nx) \tag{13}$$

There are three types of angular deviations, namely pitch, yaw, and roll. The pitch and yaw can be directly measured by a laser interferometer, while the roll angular deviation can be obtained by an electronic level instead of the laser interferometer. Many researches confirm that the angular deviations have a differential relationship with the straightness errors [20, 21]. For large machine tools, sometimes, it is hard to measure straightness errors by a laser interferometer. It will be an alternative to obtain the angular deviations first and then the straightness errors can be obtained by integrating on distance.

Squareness errors can be calculated from straightness errors. As shown in Fig. 6, the squareness error between *X*- and *Z*-axes can be calculated after the horizontal straightness errors of *X*- and *Z*-axes are obtained in the same benchmark. The S_{xz} squareness error can be expressed by Eq. (14) [22].

$$S_{xz} = \frac{\pi}{2} - \varphi + (\theta_x + \theta_z) \tag{14}$$

where θ_x and θ_z are the produced angles between reference axis and the mean straight line and φ is the edge angle of target.

3.3 Modeling results

As shown in Table 2, the positioning errors, straightness errors, and yaw errors are measured under different thermal conditions. The results indicate that the thermal effects greatly affect the positioning errors, but do not significantly influence the straightness errors or the yaw errors.

The positioning errors of the *X*- and *Z*-axes are modeled using the moderation model described in Section 3.1. The experimental results show that the temperature of the front bearing is nearly the same as that of the rear bearing; therefore, only the temperature of the front bearing is used to build the model. Here, the average of ΔT_1 and ΔT_2 is chosen as the moderator. ΔT_1 is the temperature difference between the front bearing and the ambient, while ΔT_2 is the temperature difference between the nut and the ambient.

Table 2 Measurement results of component errors

X-axis															
x/mm	0	20	40	60	80	100	120	140	160	180	200	220	240	*ΔT*1/°C	*ΔT*2/°C
δ_{xx}-1/μm	0	1.9	3.0	4.9	4.4	5.5	7.4	8.6	9.2	11.6	12.1	14.2	15.1	0	0
δ_{xx}-2/μm	0	2.8	5.6	7.1	8.0	8.7	10.1	10.9	12.8	14.6	16.0	17.3	19.6	1.2	0.9
δ_{xx}-3/μm	0	3.7	7.6	9.1	11.3	11.7	14.0	15.3	17.8	18.1	18.9	20.3	21.6	2.5	1.7
δ_{xx}-4/μm	0	4.7	9.6	11.7	14.7	16.0	17.7	18.9	20.7	20.9	22.1	23.3	23.6	4.1	3.3
δ_{xx}-5/μm	0	6.9	11.8	15.3	19.1	19.4	21.5	22.2	24.4	23.7	25.3	26.4	27.6	5.5	4.7
δ_{zx}/μm	0	2.6	3.4	2.9	4.3	5.2	4.5	6.2	7.5	5.6	7.2	6.6	7.1		
$\varepsilon_{\beta x}/_{10^{-4}}$	0	0.1	0.2	0.3	0.4	0.5	0.6	0.7	0.8	0.9	1.0	1.1	1.2		
Z-axis															
z/mm	0	25	50	75	100	125	150	175	200	225	250			ΔT1/°C	ΔT2/°C
δ_{zz}-1/μm	0	−2.5	−3.2	−6.6	−9.3	−8.8	−11.6	−12.0	−13.7	−14.2	−15.7			0	0
δ_{zz}-2/μm	0	−1.3	−1.3	−2.3	−5.2	−5.4	−7.2	−6.9	−8.6	−8.6	−9.5			2.1	1.2
δ_{zz}-3/μm	0	−0.1	−0.3	−1.1	−2.7	−2.3	−3.6	−3.5	−4.3	−4.9	−6.1			3.8	3.0
δ_{zz}-4/μm	0	1.2	1.3	1.8	1.2	0.4	1.6	1.2	0.5	1.8	1.5			5.2	4.3
δ_{zz}-5/μm	0	2.2	2.7	3.4	3.0	3.4	4.4	3.9	4.6	5.8	6.7			6.2	5.6
δ_{xz}/μm	0	−1.9	−3.1	−2.0	−4	−3.6	−5.3	−6.1	−4.9	−5.3	−4				
$\varepsilon_{\beta z}/_{10^{-4}}$	1.5	1.25	1	0.75	0.5	0.25	0	−0.25	−0.5	−0.75	−1				

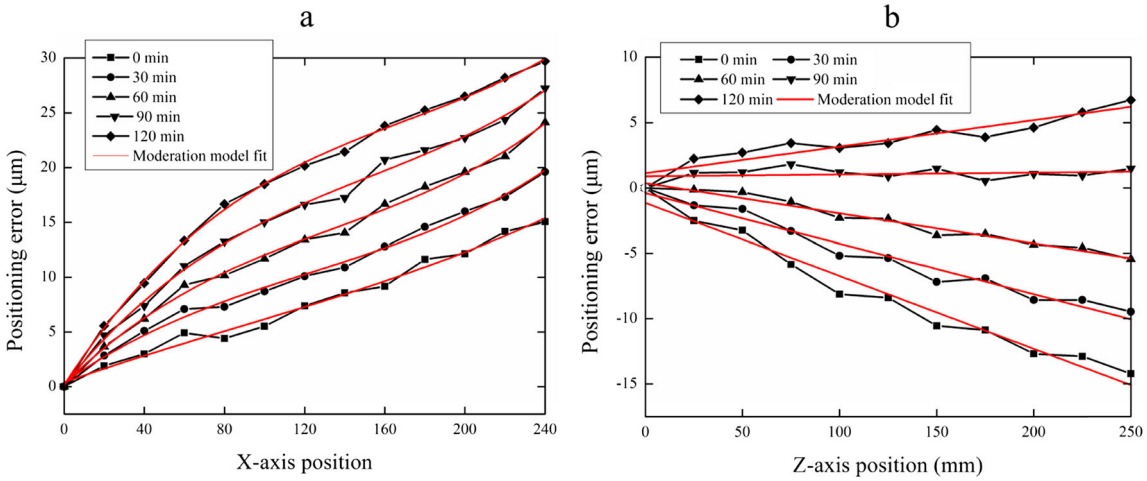

Fig. 7 Positioning error with thermal effects: **a** *X*-axis and **b** *Z*-axis

$$\Delta T_1 = t_{b1} - t_{amb},\ \Delta T_2 = t_{n1} - t_{amb} \tag{15}$$

As shown in Fig. 7, the curve slopes vary with temperature, while the curve forms remain unchanged. Therefore, a pure moderation model is selected. For the *X*-axis, the positioning error is modeled as a polynomial and that of the *Z*-axis is modeled by a linear regression. The modeling results are as shown in Eq. (16) and (17).

$$\delta_{xx} = 0.38606 + 0.06456 \cdot x - 1.08289 \times 10^{-4} \cdot x^2 + 4.1589 \times 10^{-7} \cdot x^3 + 0.00512 \cdot (\Delta T_1 + \Delta T_2) \cdot x \tag{16}$$

$$\delta_{zz} = -1.14112 - 0.05584 \cdot z + 0.00638 \cdot (\Delta T_1 + \Delta T_2) \cdot z \tag{17}$$

As shown in Fig. 8, the straightness errors of the *X*- and *Z*-axes are modeled using the Fourier series described in Section 3.2. The fourth order Fourier series is presented in Eq. (18).

$$y = a_0 + a_1\cos(x \cdot w) + b_1\sin(x \cdot w) + a_2\cos(2xw) + b_2\sin(2xw) + a_3\cos(3xw) + b_3\sin(3xw) + a_4\cos(4xw) + b_4\sin(4xw) \tag{18}$$

where a_0–a_4 and b_1–b_4 are constant coefficients.

The constant coefficients with 95 % confidence bounds for the *X*-axis straightness error are presented in Eq. (19), and those for the *Z*-axis are presented in Eq. (20).

$$a_0 = 4.351, a_1 = -2.585, b_1 = -1.006, a_2 = -1.236, b_2 = 0.5519$$
$$a_3 = -0.6514, b_3 = 0.7601, a_4 = 0.1709, b_4 = 0.9864, w = 0.02118 \tag{19}$$

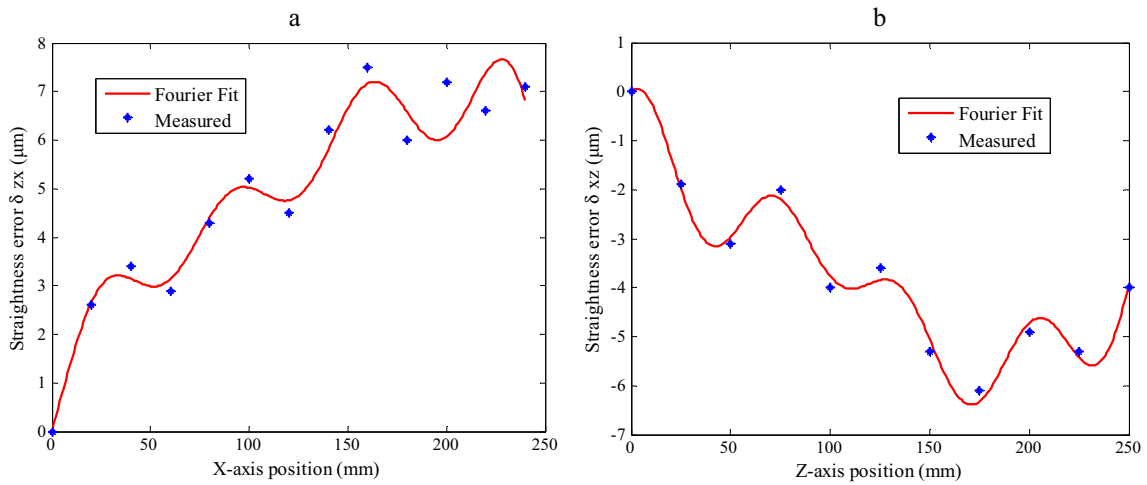

Fig. 8 Straightness error: **a** δ_{zx} and **b** δ_{xz}

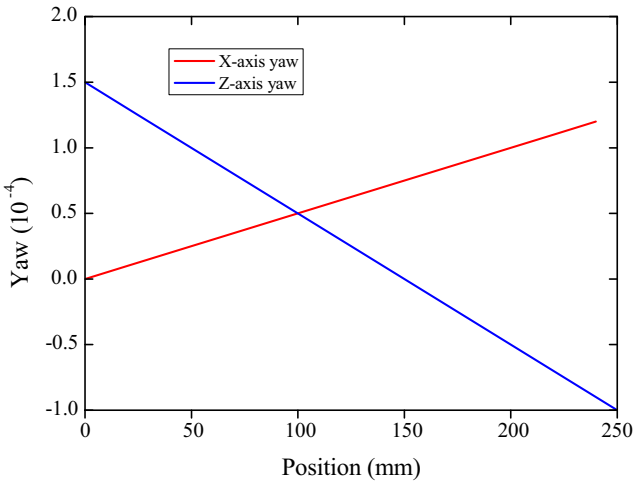

Fig. 9 Yaw errors of *X*- and *Z*-axes

$$a_0 = -3.643, a_1 = 1.435, b_1 = -1.444, a_2 = 0.6634, b_2 = 0.06968$$
$$a_3 = 0.623, b_3 = -0.1944, a_4 = 0.9285, b_4 = 0.05508, w = -0.02274 \quad (20)$$

The yaw errors of the *X*- and *Z*-axes are depicted in Fig. 9, and the modeling results are presented in Eqs. (21) and (22).

$$\varepsilon_{\beta x} = 0.005 \cdot x \times 10^{-4} \quad (21)$$

$$\varepsilon_{\beta z} = (-0.01 \cdot z + 1.5) \times 10^{-4} \quad (22)$$

Based on the straightness errors of the *X*- and *Z*-axes, the squareness of the two axes can be obtained by Eq. (14). The squareness result of the *X*- and *Z*-axes is 1.7 in.

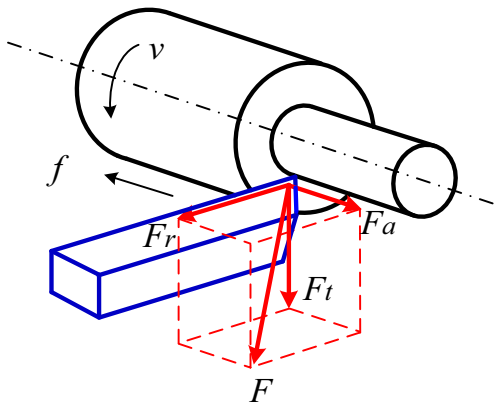

Fig. 10 Cutting force decomposition

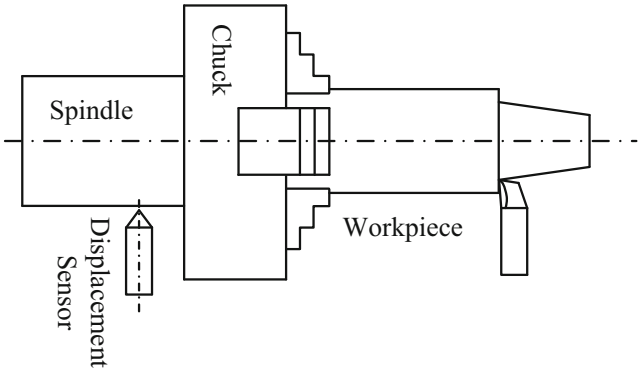

Fig. 11 Actual cutting tests for $\delta_{\text{F-spindle}}$

4 Modeling of load-induced errors

As shown in Fig. 10, the cutting force during the cutting process can be divided into three sub-forces in the *X*, *Y*, and *Z* directions. F_a is the axial force (feed force), F_r is the radial force, and F_t is the tangential force. These three forces and their torques act on the worktable, leading to contact deformations and error motions of the *X*- and *Z*-axes, namely, $\delta_{\text{F-table}}$. Meanwhile, reaction forces act on the spindle and cause spindle shifts, namely, $\delta_{\text{F-spindle}}$. Below, we separately analyze the load-induced errors $\delta_{\text{F-table}}$ and $\delta_{\text{F-spindle}}$.

4.1 Measurement and modeling of $\delta_{\text{F-spindle}}$

As shown in Fig. 11, several actual cutting tests are conducted. The spindle speed is 2000 r/min, and the feed rate varies from 100 to 200 mm/min. In these tests, a Kistler dynamometer is installed to record the cutting forces in three directions in real time. Meanwhile, the motor currents of the spindle, *X*- and *Z*-axes, are obtained by the programmable logic controller. These motor currents will be used to model the cutting forces [12]. The error $\delta_{\text{F-spindle}}$ is obtained by the displacement sensor

Table 3 Cutting forces, motor currents, and spindle shifts

Data no.	Tangential force F_t (N)	Axial force F_a (N)	Radial force F_r (N)	Spindle motor current I_s (A)	*Z*-axis motor current I_z (A)	*X*-axis motor current I_x (A)	$\delta_{\text{F-spindle}}$ (mm)
1	430	250	215	1.71	0.68	0.60	0.0059
2	442	262	220	1.72	0.70	0.60	0.0051
3	530	317	279	1.81	0.75	0.63	0.0068
4	572	380	290	1.83	0.78	0.64	0.0069
5	652	449	302	1.88	0.82	0.65	0.0075
6	670	453	348	1.89	0.83	0.69	0.0106
7	913	502	397	2.21	0.88	0.75	0.0111
8	980	528	459	2.26	0.91	0.79	0.0128
9	1070	530	470	2.33	0.91	0.81	0.0135

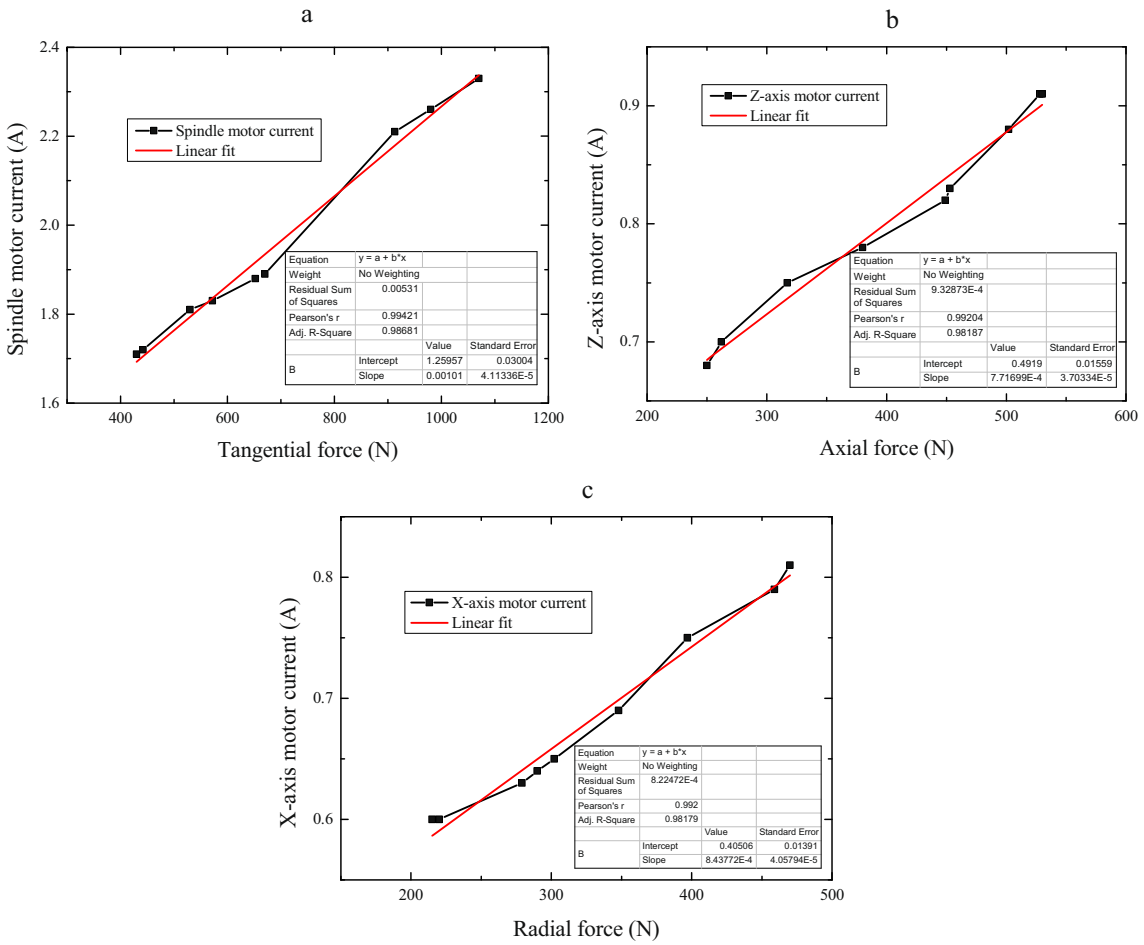

Fig. 12 Relationship between cutting force and motor current: **a** tangential, **b** axial, and **c** radial

installed on the spindle. Table 3 shows the measurement results of the cutting forces, motor currents, and spindle shifts.

The relationships between the cutting forces and related motor currents are shown in Fig. 12. The fitting results indicate approximately linear relationships between the cutting forces and the motor currents.

The relationships between the tangential force and spindle motor current, the axial force and *Z*-axis motor current, and the radial force and *X*-axis motor current are described in Eq. (23).

$$\begin{aligned} I_{\mathrm{s}} &= 0.00101 \times F_t + 1.25957 \\ I_{\mathrm{z}} &= 0.0007717 \times F_a + 0.4919 \\ I_{\mathrm{x}} &= 0.0008438 \times F_r + 0.40506 \end{aligned} \tag{23}$$

The model of $\delta_{\text{F-spindle}}$ is established in Eq. (24) as a function of three motor currents.

$$\delta_{\text{F-spindle}} = 0.0618 \times I_{\mathrm{x}} - 0.0272 \times I_{\mathrm{z}} - 0.0058 \times I_{\mathrm{s}} \tag{24}$$

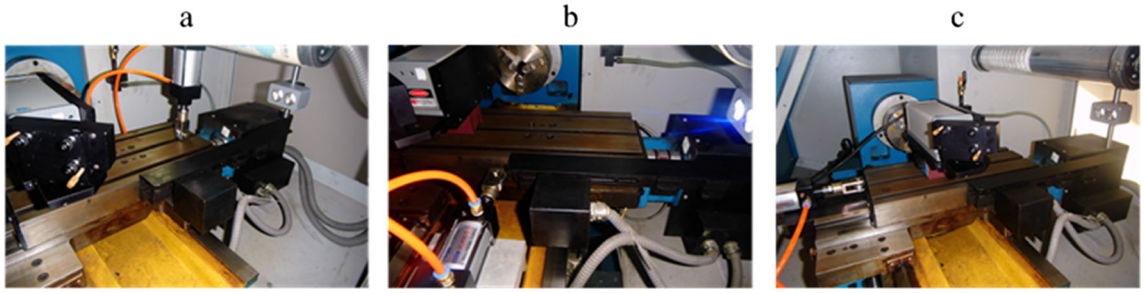

Fig. 13 Load test: **a** vertical, **b** axial, and **c** radial

4.2 Measurement and modeling of $\delta_{\text{F-table}}$

Cutting forces react on the worktable and cause error motions of the *X*- and *Z*-axes. A load test is conducted, in which a pushing cylinder is used to simulate the load, as shown in Fig. 13. The changes in error motions under different loads are determined. As described in Section 2, the error map of the lathe is in the *XZ* plane, and the major component errors are δ_{zz}, δ_{zx}, $\varepsilon_{\beta z}$, δ_{xx}, δ_{xz}, and $\varepsilon_{\beta x}$. Vertical loads applied to the slide cause the pitch error of the slide during motion. However, the error is not in the *XZ* plane and has little influence on the machining accuracy. In the test, the positioning errors, straightness errors, and yaw errors of the *X*- and *Z*-axes are measured during loading.

The changes in error motions under different loads are presented in Fig. 14. Axial loads have a large influence on δ_{zz}, δ_{xz}, and $\varepsilon_{\beta x}$, while radial loads cause deviations of δ_{zx}, $\varepsilon_{\beta z}$, and δ_{xx}. When the load point is far from the worktable center, the torque increases and the yaw error changes significantly.

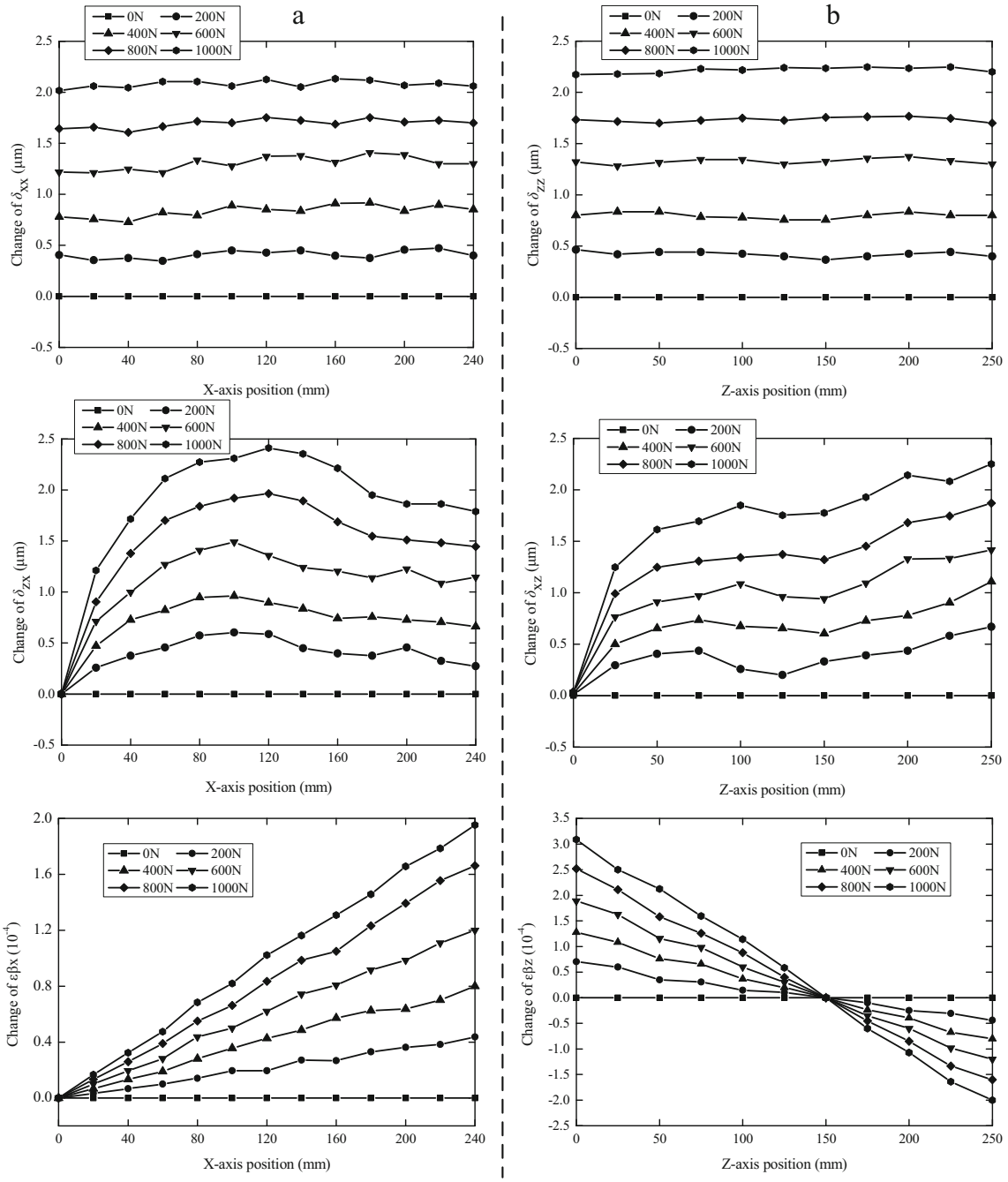

Fig. 14 Load-induced error motions: **a** *X*-axis and **b** *Z*-axis

The change in error motions can be fitted as a function of position and load. Due to the limited space, the results are not listed here. In the actual cutting process, the load on the worktable can be predicted by the motor current model, which is described by Eq. (23). Therefore, the change in error motions is a function of position and motor current. So far $\delta_{\text{F-table}}$ has been calculated.

Based on Section 4.1 and 4.2, $\delta_{\text{F-spindle}}$ and $\delta_{\text{F-table}}$ are obtained, and the flowchart of the calculating process is shown in Fig. 15. Substituting the load-induced errors into Eq. (9), the final error map of the machine tool is obtained.

5 Compensation implementation and model verification

To verify the error map with thermal and load effects, two experiments are conducted. One is a double ball bar (DBB) test without load effects, and the other consists of real cutting tests under load effects. The DBB is installed in the *XZ* plane with a radius of 100 mm. The error map is compensated by moving the *X*- and *Z*-axes according to the error vector ΔW. As shown in Fig. 16, the DBB readings indicate that the errors are reduced significantly after compensation.

Actual cutting experiments are conducted, and the workpiece sizes are measured to validate the error map modeling. Two types of workpieces, stepped shafts and tapered shafts, are machined. Each type of workpiece is divided into two groups. One group is compensated for load effects while the other group is not. In the cutting process, the final size is reached with only one cutting operation. The cutting thickness changes in the process, as do the cutting forces and cutting force-induced errors.

As shown in Table 4, when only the thermal errors are compensated, the size errors of the two workpieces are reduced by 54.3 and 62.5 %, respectively. The accuracy

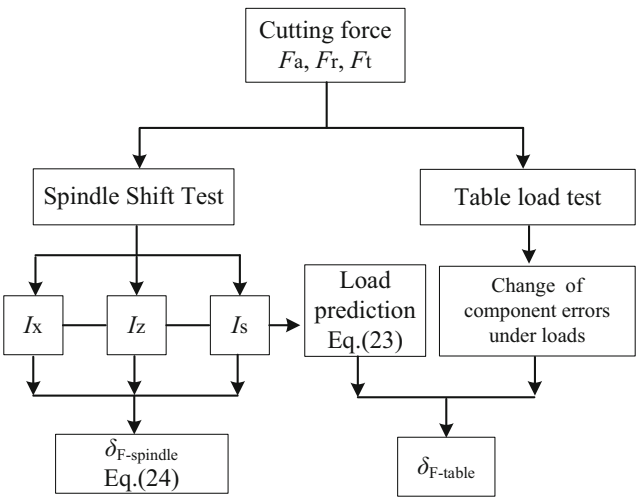

Fig. 15 Flowchart of $\delta_{\text{F-spindle}}$ and $\delta_{\text{F-table}}$ calculating process

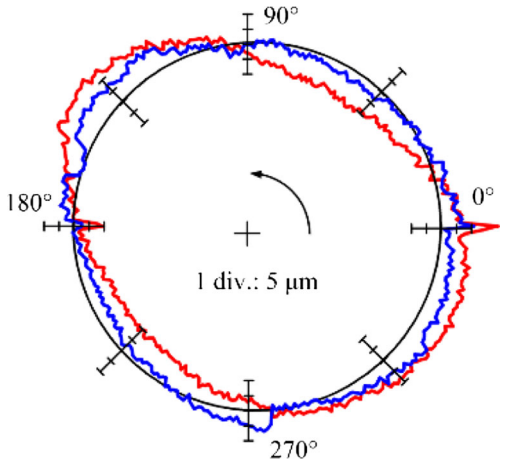

Fig. 16 Double ball bar test pre- and post-compensation. *Red*: pre-compensation; *blue*: post-compensation

increases by 10 % when the load-induced errors are simultaneously compensated.

6 Conclusions and future work

We build an error map of an NC lathe under thermal and load effects. The following conclusions can be drawn:

1. Thermal effects influence the slopes of the positioning error curves, but do not significantly change their forms. The moderation model is effective for building the positioning errors with thermal effects. The Fourier series is appropriate for modeling straightness errors.
2. The results of the actual cutting tests indicate an approximately linear relationship between the cutting forces and

Table 4 Actual cutting tests

Workpiece type	Ideal size (mm)	Without comp. No. 1	Only thermal No. 2	Thermal and load No. 3	Cutting parameters
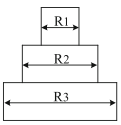	*R*1=20	19.972	19.987	19.990	*n*=2000 r/min
	*R*2=40	39.966	39.986	39.988	*f*=100 mm/min
	*R*3=60	59.958	59.979	59.983	
Average error(μm)	0	0.035	0.016	0.013	
Accuracy improvement		0 %	54.3 %	62.9 %	
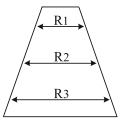	*R*1=31.547	31.502	31.528	31.535	*n*=2000 r/min
	*R*2=43.094	43.047	43.077	43.083	*f*=100 mm/min
	*R*3=54.641	54.589	54.623	54.628	
Average error(μm)	0	0.048	0.018	0.012	
Accuracy improvement		0 %	62.5 %	75 %	

the motor currents. It is proper to use motor currents to model the cutting forces.

3. A load test is conducted in which a pushing cylinder is used to simulate actual cutting forces. Vertical loads applied to the worktable cause pitch errors of the slide during motion. Axial loads have large influence on δ_{zz}, δ_{xz}, and $\varepsilon_{\beta x}$, while radial loads cause deviations of δ_{zx}, $\varepsilon_{\beta z}$, and δ_{xx}. When the load point is far from the worktable center, the torque increases, and the yaw error changes significantly.
4. When only the thermal errors are compensated, the size errors of the two workpieces are reduced by 54.3 and 62.5 %, respectively. The accuracy increases by 10 % when the load-induced errors are simultaneously compensated.

The error prediction under thermal and load effects of multi-axis machine tools will be our future work. Effective models for predicting cutting forces of the milling process are being studied.

Acknowledgments This research was sponsored by the National Science Foundation Projects of P.R. China [Nos. 51275305, 51175343], the Specialized Research Fund for the Doctoral Program of High Education [No. 20110073110041], and the Chinese National Science and Technology Key Special Projects [No. 2011ZX04015-031].

Conflict of interest The authors declare that there is no conflict of interest.

References

1. Ramesh R, Mannan MA, Poo AN (2000) Error compensation in machine tools—a review part I: geometric, cutting-force induced and fixture-dependent errors. Int J Mach Tools Manuf 40(9):1235–1256
2. Yang H, Ni J (2003) Dynamic modeling for machine tool thermal error compensation. J Manuf Sci E-T ASME 25(2):245–254
3. Wu CW, Tang CH, Chang CF, Shiao YS (2012) Thermal error compensation method for machine center. Int J Adv Manuf Technol 59(5–8):681–689
4. Lin ZC, Chang JS (2007) The building of spindle thermal displacement model of high speed machine center. Int J Adv Manuf Technol 34(5–6):556–566
5. Li Y, Zhao W, Wu W, Lu B, Chen Y (2014) Thermal error modeling of the spindle based on multiple variables for the precision machine tool. Int J Adv Manuf Technol 72(9–12):1415–1427
6. Creighton E, Honegger A, Tulsian A, Mukhopadhyay D (2010) Analysis of thermal errors in a high-speed micro-milling spindle. Int J Mach Tools Manuf 50(4):386–393
7. Zhang J, Feng P, Chen C, Yu D, Wu Z (2013) A method for thermal performance modeling and simulation of machine tools. Int J Adv Manuf Technol 68(5–8):1517–1527
8. Zhang Y, Yang JG, Xiang ST, Xiao HX (2013) Volumetric error modeling and compensation considering thermal effect on five-axis machine tools. Proc IMechE, Part C: J Mech Eng Sci 227(5):1102–1115
9. Liu YL, Lu Y, Gao D, Hao ZP (2013) Thermally induced volumetric error modeling based on thermal drift and its compensation in Z-axis. Int J Adv Manuf Technol 69(9–12):2735–2745
10. Furukawa Y, Moronuki N (1987) Contact deformation of a machine tool slideway and its effect on machining accuracy: vibration, control engineering, engineering for industry. JSME I J: Bull JSME 30(263):868–874
11. Yang S, Yuan J, Ni J (1997) Real-time cutting force induced error compensation on a turning center. Int J Mach Tools Manuf 37(11):1597–1610
12. Wu H, Chen HJ, Meng P, Yang JG (2010) Modelling and real-time compensation of cutting-force-induced error on a numerical control twin-spindle lathe. Proc I MechE Part B: J Eng Manuf 224(4):567–577
13. Fan KC, Chen HM, Kuo TH (2012) Prediction of machining accuracy degradation of machine tools. Precis Eng 36(2):288–298
14. Xiang ST, Zhu XL, Yang JG (2014) Modeling for spindle thermal error in machine tools based on mechanism analysis and thermal basic characteristics tests. Proc I MechE Part C: J Mech Eng Sci 228(18):3381–3394
15. Lu YX, Islam MN (2012) A new approach to thermally induced volumetric error compensation. Int J Adv Manuf Technol 62(9–12):1071–1085
16. Ramesh R, Mannan MA, Poo AN (2000) Error compensation in machine tools—a review part II: thermal errors. Int J Mach Tools Manuf 40(9):1257–1284
17. Cohen J, Cohen P, West SG, Aiken LS (2003) Applied multiple regression/correlation analysis for the behavioral sciences (3rd ed.). Mahwah, NJ: Erlbaum
18. Durand RM, Sharma S, Gur-Arie O (1981) Identification and analysis of moderator variables. J Mark Res 18(3):291–300
19. Uriarte L, Zatarain M, Axinte D, Yague-Fabra J, Ihlenfeldt S, Eguia J, Olarra A (2013) Machine tools for large parts. CIRP Ann Manuf Technol 62(2):731–750
20. Ekinci TO, Mayer JRR (2007) Relationships between straightness and angular kinematic errors in machines. Int J Mach Tools Manuf 47(12–13):1997–2004
21. Liao JS, Lai JM, Chieng WH (1997) Modeling and analysis of nonlinear guideway for double-ball bar (DBB) measurement and diagnosis. Int J Mach Tools Manuf 37(5):687–707
22. Lee JH, Yang SH (2005) Measurement of geometric errors in a miniaturized machine tool using capacitance sensors. J Mater Process Tech 164–165:1402–1409